



A novel methodology for non-linear system identification of battery cells used in non-road hybrid electric vehicles



Johannes Unger ^{a,*}, Christoph Hametner ^a, Stefan Jakubek ^a, Marcus Quasthoff ^b

^a Vienna University of Technology, Institute for Mechanics and Mechatronics, A-1040 Vienna, Austria

^b Liebherr Machines Bulle SA, CH-1630 Bulle, Switzerland

HIGHLIGHTS

- A generic methodology for battery cell terminal voltage modeling is presented.
- Model based experiment design is introduced for optimal battery cell testing.
- The optimal excitation signals cover the entire operating ranges of non-road HEVs.
- The framework is purely data-based and regards relaxation and hysteresis effects.
- Measurements validate the methodology applicable to different cell chemistries.

ARTICLE INFO

Article history:

Received 12 September 2013

Received in revised form

1 July 2014

Accepted 3 July 2014

Available online 11 July 2014

Keywords:

Non-linear system identification

Local model networks (LMN)

Battery cell model

Design of experiments (DoE)

Fisher information

Lithium-ion chemistries

ABSTRACT

An accurate state of charge (SoC) estimation of a traction battery in hybrid electric non-road vehicles, which possess higher dynamics and power densities than on-road vehicles, requires a precise battery cell terminal voltage model. This paper presents a novel methodology for non-linear system identification of battery cells to obtain precise battery models. The methodology comprises the architecture of local model networks (LMN) and optimal model based design of experiments (DoE). Three main novelties are proposed: 1) Optimal model based DoE, which aims to high dynamically excite the battery cells at load ranges frequently used in operation. 2) The integration of corresponding inputs in the LMN to regard the non-linearities SoC, relaxation, hysteresis as well as temperature effects. 3) Enhancements to the local linear model tree (LOLIMOT) construction algorithm, to achieve a physical appropriate interpretation of the LMN. The framework is applicable for different battery cell chemistries and different temperatures, and is real time capable, which is shown on an industrial PC. The accuracy of the obtained non-linear battery model is demonstrated on cells with different chemistries and temperatures. The results show significant improvement due to optimal experiment design and integration of the battery non-linearities within the LMN structure.

© 2014 Elsevier B.V. All rights reserved.

1. Introduction

A novel generic methodology for non-linear system identification and optimal model based design of experiments (DoE) of battery cells are proposed in this paper.

The control strategy of hybrid electric vehicles (HEV) is essentially dependent on the state of charge (SoC) of the used traction battery. The state of charge of the battery is not measurable on-line,

which requires an estimate of the actual SoC during operation [1]. The estimation of the SoC is placed in the battery management system (BMS) and is often only based on the open circuit voltage of the battery. This leads to big estimation errors, since the non-linear behavior of the battery voltage at operation is not regarded with this approach [2]. Another approach is to integrate the battery current. Disadvantageously, current offsets are accumulated, which may lead to estimation errors after some time. The third possibility is to use SoC estimators (e.g. extended Kalman filter), which require a model of the battery that can be implemented in the BMS in real time. The model is an integral part of the BMS and describes the non-linear dynamic behavior of the battery cell terminal voltage. The SoC estimation accuracy can be improved only if a precise non-linear battery cell model is used in the SoC estimator [3].

* Corresponding author.

E-mail addresses: unger@impa.tuwien.ac.at (J. Unger), hametner@impa.tuwien.ac.at (C. Hametner), jakubek@impa.tuwien.ac.at (S. Jakubek), marcus.quasthoff@liebherr.com (M. Quasthoff).

Non-road hybrid electric vehicles and machinery (e.g. construction site vehicles, mining vehicles, ...), compared to on-road vehicles, usually demand higher power densities and load dynamics, which makes the modeling of the batteries more complicated [4]. The non-linear battery effects (e.g. hysteresis, relaxation, temperature effects, ...) of electrochemical batteries are increased due to the high power densities [5].

In this paper, a non-linear data-based battery model is proposed, which can be used for the purpose of accurate SoC estimation in *non-road* vehicles. Optimal model based DoE is utilized to optimize the excitation signals for battery measurements. The optimal excitation signals are used for the model parameter identification to increase the accuracy at high dynamic demands. Furthermore, due to the experiment design and data-based structure, the model can be obtained for different battery cell chemistries within a reasonable time period.

State-of-the-art battery models and DoE are reviewed in the following. The solution approach and the contributions of the paper are summarized at the end of this section.

1.1. State-of-the-art

In the literature three main types of battery model approaches are mentioned:

1. Equivalent circuit models
2. Electrochemical battery models
3. Data-based battery models.

Equivalent circuit models (ECM), as depicted in Fig. 1 exemplarily, use basic electric elements in order to model a battery cell. The main intention is to parameterize the model using physically interpretable values. Gao et al. [5] used an ECM with one RC circuit, that accounts for non-linear equilibrium potentials, rate- and temperature-dependencies, thermal effects and response to transient power demand. Pattipati et al. [6] used a modified equivalent circuit model for SoC, state-of-health (SoH) and remaining useful life estimation in the BMS. The high power density application in automotive industry requires to consider the behavior of the impedance elements (such as solution resistance, charge transfer resistance, and Warburg impedance) in a simple ECM (see Gomez et al. [7]).

Electrochemical battery models pursue to physically model the electrochemical behavior of the battery. These models are able to simulate the chemical states of a battery accurately and to give insight into the system itself [8], while the disadvantage is that they are computationally intensive. Doyle et al. [9] modeled a lithium battery cell by using concentrated solution theory. Partial differential-algebraic equations are used by Klein et al. [8] for state estimation. Santhanagopalan et al. [10] used a single particle model (SPM) for SoC estimation with an extended Kalman filter. However,

due to non-consideration of spatial variation of the states in the battery cell, the success of the SPM model, especially at high currents or long duration pulses, might not be valid for the operating region encountered for HEV [11].

Data-based models are a useful way for modeling and estimation purposes, although in general, the model parameters are not physically interpretable [8]. Plett [12,13,3], used a data-based non-linear state space model for extended Kalman filter SoC estimation. The model takes different current directions into account and regards a “hysteresis state” as well as the relaxation using a low pass filter on the current. Battery cell chemistry independence of the model is assumed. Charkhgard et al. [14] applied neural networks to battery modeling. Based on a stochastic fuzzy neural network [15,16,17], Wang et al. [18] modeled the non-linear dynamics of current, temperature and SoC to the battery voltage. Xu et al. [19] used the same model for SoC estimation. Hametner et al. [1] applied a local model network (LMN) to battery modeling. A LMN is composed of several local models that are linear in their model parameters and have a certain area of validity defined by validity functions (see e.g. Refs. [20,21,22]). The model output is non-linear, due to the non-linear interpolation of the local linear models (LLM). The LMN is constructed by an iterative algorithm, which starts with one global linear model and adds a LLM to the network in every iteration until a certain threshold is reached (partitioning). The validity of the new LLM lies in a specific form in the partition space of the model and depends on the algorithm's strategy.

All of the mentioned battery models require measurements to parameterize the model parameters. The measurements are obtained by applying a current excitation signal to a battery cell and recording the voltage response. Kroeze et al. [23] used simple constant discharge and charge cycles for the identification of an ECM, while Gao et al. [5], Chen et al. [24] and Hentunen et al. [25] made use of a discharge pulse excitation signal for the same purpose. A discharge pulse excitation signal is also used in Ref. [26] for a model-based estimation of an electrochemical battery cell model. More advanced ECM (e.g. linear parameter varying models) are identified in Refs. [27,28,13] using a pulse profile, regarding charge and discharge mode. Hu et al. [29] employs an asymmetrical current step profile, in order to cover a wide range of SoC as well as a wide current range. This profile is more dynamic compared to the other excitation signals. An example for low dynamics in non-road applications is the dynamic Federal Urban Driving Schedule (FUDS), which is used in many papers as validation signal (see e.g. Refs. [30,19,23,31]).

Depending on the model approach, the design of the experiment plays an important role since the excitation signal has a decisive influence on the parameter estimation, especially for data-based model approaches [4,1]. Model based design of experiments can be used to create optimal excitation signals: The goal is that, based on a prior model of the process (reference model), the information obtained from measurements is maximized and parameters can be estimated with minimum variance [32]. In this context, the Fisher information matrix \mathcal{I} (FIM), a way to measure the information content of a signal, is often used for optimization of an excitation signal. Furthermore, constraints of the process can be regarded, provided that the reference model is sufficiently accurate.

In Ref. [33], a local model network based generation algorithm for static experiment design is proposed. Dynamic experiment design for multilayer perceptron networks by choosing optimal inputs from a candidate set is proposed in e.g. Refs. [34,35]. Stadlbauer et al. [36,37] focused on the dynamic design of experiments based on multilayer perceptron networks. Based on these papers, Hametner et al. [38] proposed a design approach for non-linear dynamic experiments, which is targeted to minimize the model

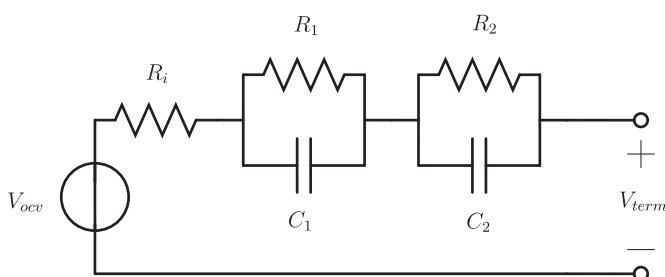


Fig. 1. Equivalent circuit model with two RC-elements.

variance of dynamic multilayer perceptron networks as well as local model networks. In Ref. [4] the benefit of model based design of experiments on battery modeling is investigated and compared with a dynamic excitation signal from the literature. Based on a linear dynamic model and predefined current levels, in Ref. [1], model based design of experiments is proposed for optimal SoC excitation and minimal measurement duration.

1.2. Solution approach

In this paper, to achieve the required accuracy of the battery cell terminal voltage model for non-road application, the data-based LMN approach is used. The advantages of the LMN are that expert knowledge can be included, the computational effort is low, no random initialization of the parameters is needed and the LLMs can be interpreted as local linearization of the process [39,40]. The LMN is constructed using the local linear model tree (LOLIMOT) algorithm, while the LMN structure is defined by corresponding inputs, which are adapted to regard the battery non-linearities SoC, relaxation and hysteresis as well as temperature and current in the model. Furthermore, to achieve a physically appropriate network, the LOLIMOT algorithm is adapted to start with a prepartitioned network and is prohibited to split the network within specified dimensions. The resulting battery cell model is, due to less computational complexity, real time capable and can be obtained for different cell chemistries.

For the reduction of the identified model parameter variance, optimal model based design of experiments is utilized to maximize the information content of measurements. The goal is to sufficiently excite the system dynamics and cover the entire SoC range during measurement, while relaxation and hysteresis effects are regarded additionally. The optimization of the excitation signal is based on a scalar cost function $J(\mathcal{I})$ and is focused on real load ranges that are frequently used in operation. Since battery constraints on current, voltage and SoC need to be regarded, a constrained optimization problem results. The optimization problem is solved using a gradient based algorithm.

The generic methodology of non-linear battery model identification is validated by means of real measurements on different battery cells. The cell chemistry independence is shown on different cell chemistries and the temperature dependence is presented for a relevant temperature range in non-road application between 12.5 °C and 35 °C.

In summary the main contributions of this paper are:

- A generic methodology for non-linear system identification applicable for different battery cell chemistries and different temperatures.
- The integration of corresponding inputs in a LMN to regard non-linear battery effects such as SoC, relaxation, hysteresis as well as current and temperature within the battery cell terminal voltage model.
- Enhancements of the LOLIMOT construction algorithm to use a prepartitioned network instead of one global model and to prohibit splitting within specified partitioning dimensions.
- Optimal model based DoE to create high dynamic excitation signals to significantly increase the battery model accuracy at high dynamic (non-road) applications.
- A real load cycle analysis for identification of frequently used load ranges in operation to focus the excitation signal optimization at these ranges.

The remainder of this paper is structured as follows: In Section 2 the LMN approach for battery modeling is described. In Section 3 the optimal model based DoE is presented. In Section 4 the

improvement by optimal model based DoE, the comparison of different LMN structures and the dynamic accuracy of the proposed battery model are demonstrated. A conclusion is made in Section 5.

2. Battery modeling using local model network

The goal of this section is to develop a generic methodology for non-linear identification of high dynamic, current–voltage battery cell models, which regard non-linear battery effects such as SoC, relaxation, hysteresis and temperature as well as current effects.

The remainder of this section is as follows: First the general architecture and structure of LMN is described. Then the construction of the LMN using the LOLIMOT algorithm is explained and finally the battery model, based on the LMN structure, is developed.

2.1. General architecture and structure of LMN

The local model network structure is basically an interpolation of local linear models, which are only valid in a certain operation regime. The underlying model structure of the LLM is chosen to be autoregressive with exogenous input. Based on the global non-linear model output \hat{y} , the global parameter vector θ and the input variables u_l , the regression vector ϕ can be arranged as

$$\begin{aligned} \phi(k, \theta) &= [\bar{y} \ \bar{u}_1 \dots \bar{u}_q \ 1]^T, \\ \bar{y} &= [\hat{y}(k-1, \theta) \dots \hat{y}(k-n, \theta)], \\ \bar{u}_l &= [u_l(k-d) \dots u_l(k-d-m_l)], l = 1, \dots, q, \end{aligned} \quad (1)$$

where k is the actual time instant, n is the output order, m_l is the input order of the l -th of q input variables and d is the dead time. The input variables u_l span the so-called input space \mathcal{Q} of the model [41] and the one in Eq. (1) regards the bias. Note that the local models are depicted for MISO systems, but in general MIMO systems are possible as well [40].

The optimal model order of the inputs and outputs can be identified by different methods: The theory behind goodness-of-fit (GOF) techniques as well as recommendations for different GOF techniques are given in Ref. [42]. GOF methods from the statistical point of view are discussed in Ref. [43]. A trade-off between the goodness-of-fit and the model complexity is provided by Akaike's information criterion, which is used in e.g. Ref. [44] to find the optimal order of an ARX structured battery model. In this paper, in order to obtain the optimal model order, the methodology proposed in Ref. [45] is used. Different selections of the model order are analyzed by the mean squared error and the best compromise between complexity and accuracy is chosen. The obtained model orders are given in the results section.

The output \hat{y}_i of the i -th of M LLMs is calculated by

$$\hat{y}_i(k, \theta) = \phi^T(k, \theta) \vartheta_i, \quad (2)$$

where $\theta = [\vartheta_1 \dots \vartheta_M]^T$ is the global parameter vector of all M local parameter vectors ϑ_i . The weighted aggregation of the local model outputs forms the global non-linear LMN output, which is obtained by

$$\hat{y}(k, \theta) = \sum_{i=1}^M \hat{y}_i(k, \theta) \Phi_i(k), \quad (3)$$

where $\Phi_i(k)$ is the validity function of the i -th LLM. The validity function is calculated by

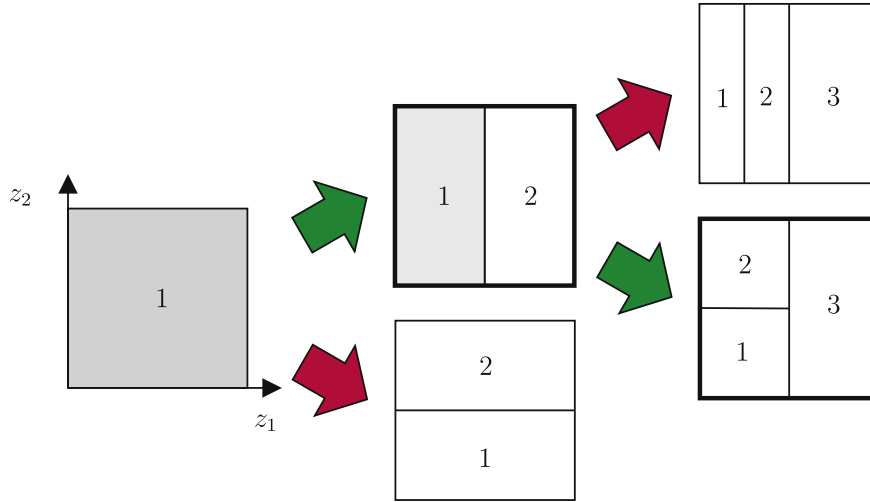


Fig. 2. LOLIMOT scheme for two-dimensional partition space.

$$\Phi_i(k) = \frac{\mu_i(k, \mathbf{z})}{\sum_{j=1}^M \mu_j(k, \mathbf{z})}, \quad (4)$$

where $\mu_i(k, \mathbf{z})$ is a Kernel function for which different common functions (e.g. uniform, triangle, ...) can be used [40] and $\mathbf{z} = [z_1 \dots z_\phi]$ includes all actual partition variables. The normalization is required in order to obtain the sum of all validity functions to be equal to 1. The ϕ partition variables in \mathbf{z} span the so-called partition space \mathcal{Z} of the model [22]. The partition space \mathcal{Z} is not mandatory the input space \mathcal{Q} [46], though input and partition variables may be the same.

2.2. Construction of LMN using LOLIMOT

In this paper, the construction of the local model network is done by the local linear model tree algorithm presented in Ref. [40]. LOLIMOT divides the partition space by axis-orthogonal splits [41]. Iteratively, the worst LLM is identified by the quadratic error criterion and is split into two new LLM in the dimension with the best improvement for the global model output, until a certain threshold is reached. Here, the threshold is the maximal number of LLM M .

The parameters for the local linear models are obtained by using weighted least squares (WLS). In order to avoid numerical effects, all input, partition and output variables are normalized from 0 to 1 [40]. In Fig. 2, the procedure is depicted for a two-dimensional partition space with more detail: In every iteration, the worst LLM is identified and is then split in all possible dimensions. All divisions are checked by the quadratic evaluation criterion and the best alternative is chosen.

In the LOLIMOT algorithm, the Kernel function $\mu_i(k, \mathbf{z})$ is chosen to be Gaussian [40], which is calculated by

$$\mu_i(k, \mathbf{z}) = \exp \left(-\frac{1}{2} \left(\frac{(z_1(k) - c_{i1})^2}{\sigma_{i1}^2} + \dots + \frac{(z_\phi(k) - c_{i\phi})^2}{\sigma_{i\phi}^2} \right) \right). \quad (5)$$

In case of axis-orthogonal splits of the partition space \mathcal{Z} , c_{ij} can be interpreted as center point of the LLM and σ_{ij} is the individual standard deviation. The standard deviation can be approximated by $\sigma_{ij} = k_{\sigma,j} \Delta_{ij}$, where Δ_{ij} is the spread of the LLM and $k_{\sigma,j}$ is a sharpness factor. The kernel function sharpness $k_{\sigma,j}$ is defined by the user and can be interpreted as an overlapping factor of the LLM that

influences the smoothness of the non-linear model output. Note that the optimal sharpness factor depends on the specific application and is different for the partitioning dimensions. The chosen sharpness factors $k_{\sigma,j}$ are given in the results section.

Alternatively, Jakubek et al. [47] presented an iterative construction algorithm for LMN, where a statistical criteria along with regularization is used in order to allow an arbitrary orientation and extent in the partition space. In Ref. [48], a residual from generalized total least squares parameter estimation is used in an expectation–maximization algorithm for proper partitioning of the LMN.

Note that, LOLIMOT has less implementation complexity due to the axis orthogonal orientation compared to the arbitrary orientation in the partition space of the mentioned alternatives and is therefore used in this paper.

2.3. Battery modeling using LMN

In this section, the LMN is adapted for battery modeling. In the following, corresponding inputs to regard the non-linear battery effects in the LMN structure and the LMN structure itself are presented. Furthermore, the enhancements for the LOLIMOT algorithm are explained to increase the physical meaning of the battery model. Fig. 3 depicts the flowchart of the battery model construction process.

2.3.1. Corresponding LMN inputs of non-linear battery effects

In general, distinction must be made between physical and chemical non-linear effects in electrochemical batteries.

In Subplot (a) in Fig. 4, constant charge as well as discharge curves for different C-rates,¹ measured on a lithium polymer (Cell A) and lithium iron phosphate (Cell B) chemistry, are depicted over the SoC. The SoC is obtained by integration of the cell current [31] and the open circuit voltage (OCV) is estimated by interpolation between the charge and discharge curve [49]. In Subplot (b) a current step sequence at different temperatures for Cell B is depicted.

The non-linear physical influence of current and temperature are observable in Subplot (b) in Fig. 4. The current applied to the battery cell changes the battery voltage dynamically, while the temperature affects the value of the internal resistance of the

¹ The C-rate is the quotient of current [A] and battery cell capacity [Ah].

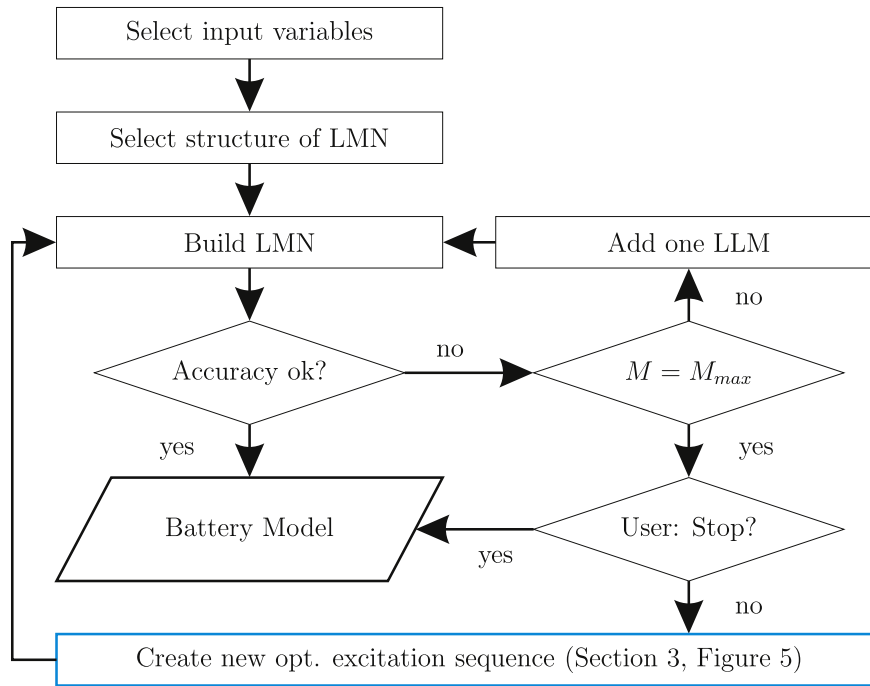


Fig. 3. Flowchart of battery model construction process.

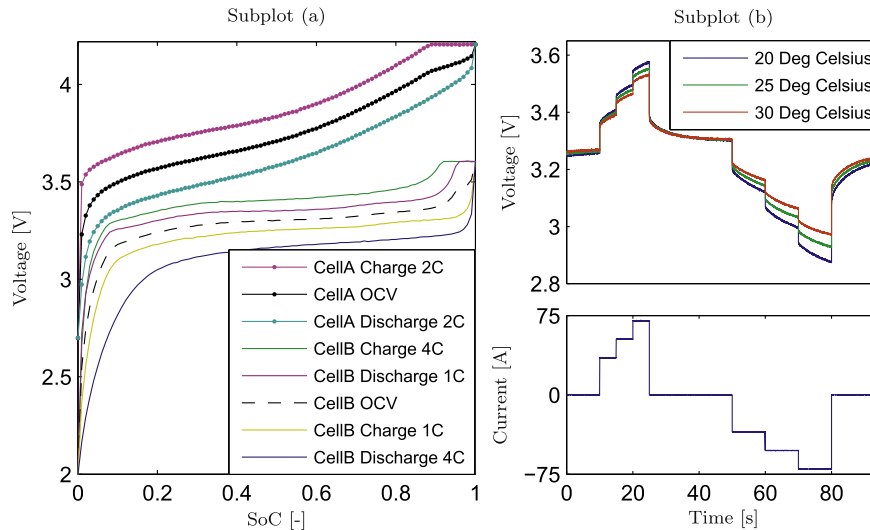


Fig. 4. Subplot (a): Discharge and charge curves for a lithium polymer (Cell A) and lithium iron phosphate (Cell B) chemistry at different currents. The open circuit voltage (OCV) is estimated by interpolation between the charge and discharge curve. Subplot (b): Voltage response of a current step sequence, similar to [29], at different temperatures for Cell B.

battery cell. Due to lower/higher temperature, increased/decreased internal resistance leads to bigger/smaller voltage drops if current is applied to the battery cell. Hence, the current as well as temperature, which are physically measurable on-line, are regarded by the corresponding inputs u_{Current} and z_{Temp} , respectively. Note that, temperature gradients are small compared to gradients of the current and therefore, it is assumed that the temperature influences the voltage behavior only statically.

From Subplot (a) in Fig. 4, the non-linear influence of the SoC on the battery cell voltage is observable. Therefore the SoC is regarded by the corresponding input z_{SoC} , which is the actual value of the SoC. The SoC can be obtained by integration of the current or alternatively by state estimation (see e.g. Refs. [1,3]). Note here, that the SoC can only be changed by the current and

thus the influence on the system behavior is assumed to be static only.

The dynamic chemical effect, referred to relaxation, is not directly measurable. It can be observed in Subplot (b) in Fig. 4 at standby current, where the voltage is slightly converging to a steady state value [13]. The time axis of the time constants for relaxation and current effects are very different. Note that, relaxation also acts during current phases [50]. Following Ref. [13], the relaxation non-linearity can be approximated using a low pass filter on the current, which need to fulfill certain requirements:

- After a long rest period and
- during constant-current discharge/charge, the relaxation state needs to converge to zero.

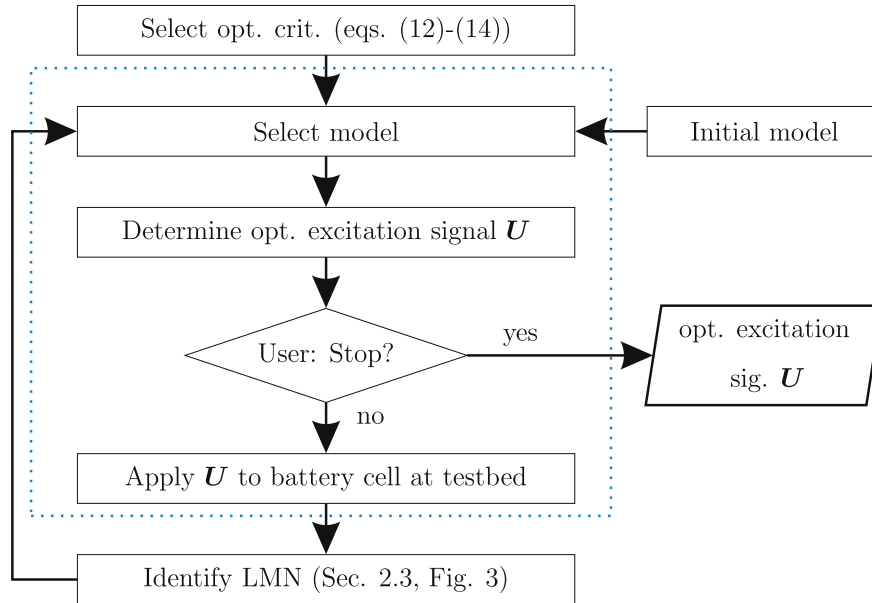


Fig. 5. Process flowchart of the DoE to obtain the optimal excitation signal U . Compare blue block with battery model identification flowchart in Fig. 3. (For interpretation of the references to colour in this figure legend, the reader is referred to the web version of this article.)

The relaxation input is realized by the dynamic corresponding input

$$u_{\text{Relax}} = \text{filt}(\Delta u_{\text{Current}}), \quad (6)$$

where $\Delta u_{\text{Current}}$ describes the change rate of the current, in order to force zero DC-gain of the filter $\text{filt}(\cdot)$. In this paper, the filter is designed as a third order low pass filter with appropriate chosen relaxation time constant of the battery cell. The time constant of the relaxation is approximated properly on the basis of the voltage converging speed at standby current after a current pulse have been applied to the battery cell.

In Fig. 4 in Subplot (a) at 10% SoC and in Subplot (b) at standby current, different shapes of the charge and discharge curve are observable. This chemical non-linear effect is referred to as hysteresis [51]. A first order hysteresis input is used as corresponding input z_{Hyst} for the hysteresis effect. The value is obtained by the $\text{sign}(\cdot)$ of the current and is kept at the last value, if the current is zero.

Other known chemical effects, e.g. intercalation effects, conductivity of anode/electrolyte/cathode or concentration gradients, which are not directly observable in Fig. 4, are neglected due to marginal influence compared to the mentioned effects.

2.3.2. LMN structure of battery models

In order to integrate the corresponding inputs to the LMN structure, it is necessary to distinguish between static and dynamic influence on the cell voltage. The dynamic corresponding inputs need to be included in the input space \mathcal{Q} to be inputs of the dynamic LLM. The static corresponding inputs are included in the partition space \mathcal{Z} to be used for partitioning. Based on this differentiation and the mentioned battery effects, the partition as well as input space can be denoted by

$$\begin{aligned} \mathcal{Z} &= [z_1 \ z_2 \ z_3] \triangleq [z_{\text{SoC}} \ z_{\text{Hyst}} \ z_{\text{Temp}}], \\ \mathcal{Q} &= [u_1 \ u_2 \ u_3] \triangleq [z_{\text{SoC}} \ u_{\text{Current}} \ u_{\text{Relax}}]. \end{aligned} \quad (7)$$

In order to regard the continuous change of the voltage depending on the SoC, the static SoC input z_{SoC} is additionally

regarded in the input space \mathcal{Q} . Note that, for observability of the SoC using a Fuzzy-Observer, the SoC is also required to be an input of the model (c.f. [1]).

2.3.3. User defined prepartitioning of the LMN structure for battery models

The choice of the initial partitions of \mathcal{Z} used in the LOLIMOT algorithm, influences the partitioning decision significantly. In order to prevent physically inappropriate partitions, the LOLIMOT algorithm is forced to start with predefined physically appropriate partitions, instead of one global partition. Furthermore, selected dimensions of the partition space are prohibited to be split. This has the advantage of reducing the computational efforts and keeps all partitions physically appropriate.

The hysteresis input z_{Hyst} refers to the corresponding cell polarization and is therefore split into charge as well as discharge mode. Further partitioning within this dimension is prohibited. Based on Subplot (b) in Fig. 4, the temperature influence within 12.5 °C and 35 °C is assumed to be evenly distributed. Therefore, the temperature dimension is split into three partitions and partitioning is also prohibited, because a simultaneous split of charge and discharge mode cannot be achieved due to the split in the hysteresis dimension. The number of initial partitions is therefore 6, while the partitioning degree of freedom is limited to the SoC dimension. Alternatively, expert knowledge can be used to set up an appropriate prepartitioned network.

3. Optimal model based design of experiments

The goal of an optimal battery excitation signal is, that the system dynamics are sufficiently excited and the entire SoC range is covered during measurement, while relaxation and hysteresis effects are regarded additionally. Batteries are tested by applying a load current excitation signal U to a battery cell and the cell voltage is recorded. Usual excitation signals, e.g. Ref. [29], apply intermediate current steps for dynamic excitation of the battery cell. Non-road applications usually require higher dynamic excitation signals to sufficiently include high dynamic system behavior within the measurements [4].

For that purpose, optimized high dynamic excitation sequences are created by optimal model based design of experiments. Relaxation, hysteresis as well as constant current behavior are additionally regarded by constant discharge/charge current with following standby current in front of/after the optimized high dynamic excitation sequence. The entire SoC operating range is covered by merging optimized excitation sequences for evenly distributed SoC values across the SoC operating range.

In the following, the optimization of the dynamic excitation sequence based on optimal model based design of experiments by simultaneously regarding the battery constraints is discussed. Optimality criteria, based on the Fisher information matrix \mathcal{I} , are formulated and optimized by a gradient based algorithm. Load ranges frequently used in operation are identified by real load cycle analysis and are regarded in the optimization in order to improve the obtained model quality especially for these ranges. At the end, the extensions on the excitation sequence are described in detail.

3.1. Formulation and calculation of optimization criteria

The methodology of optimal model based design of experiments is used to create excitation signals for identification of models with minimum parameter variance. According to Ref. [38], an excitation signal \mathbf{U} can be optimized using the FIM, which can only be improved by modification of the system inputs. The calculation of \mathcal{I} is based on the partial derivative of the model output with respect to the model parameters. For the LMN battery model described in the last section, the parameter sensitivity vector $\psi(k)$ can be denoted by

$$\psi(k) = \frac{\partial \hat{y}(k, \theta)}{\partial \theta} = \begin{bmatrix} \Phi_1(k) \varphi(k, \theta) \\ \vdots \\ \Phi_M(k) \varphi(k, \theta) \end{bmatrix}, \quad k = 1, \dots, N, \quad (8)$$

where M denotes the number of LLM and $\Phi_i(k)$, $\varphi(k, \theta)$, θ as defined in (4) and (1). The reference model can be obtained by two possibilities:

- A LMN model is available.
- A different model (no LMN model) is available.

In this paper, a linear model of the battery, which corresponds to a LMN with only one LLM, is identified by an a priori available excitation signal and is further used in the following. In case of an available complex electrochemical simulation model, simulation results can be used to identify a LMN as a reference model, alternatively. Nevertheless, this paper should show, that the easy approach of a linear model already increase the model quality significantly.

The FIM, which is based on $\psi(k)$, can be defined by

$$\mathcal{I} = \frac{1}{\sigma^2} \sum_{k=1}^N \underbrace{\frac{\partial \hat{y}(k, \theta)}{\partial \theta}}_{\psi(k)} \frac{\partial \hat{y}(k, \theta)}{\partial \theta}^T, \quad k = 1, \dots, N, \quad (9)$$

where σ is the variance of the measurement noise [52]. Using a compact notation for the parameter sensitivity matrix

$$\Psi = [\psi^T(1) \dots \psi^T(N)]^T, \quad (10)$$

the FIM can be denoted by

$$\mathcal{I} = \frac{1}{\sigma^2} \Psi^T \Psi. \quad (11)$$

For the optimization of the excitation sequence, scalar criteria, all based on the Fisher information matrix \mathcal{I} , are formulated. Three common criteria exist [52]:

$$\text{A – optimality : } J_A = \text{Tr}(\mathcal{I}^{-1}) \rightarrow \min_{\mathbf{U}} \quad (12)$$

$$\text{D – optimality : } J_D = \det(\mathcal{I}) \rightarrow \max_{\mathbf{U}} \quad (13)$$

$$\text{E – optimality : } J_E = \lambda_{\min}(\mathcal{I}) \rightarrow \max_{\mathbf{U}} \quad (14)$$

The trace of the inverse of the Fisher information matrix is subject to minimization for A-optimality, D-optimality is targeted to maximize the determinant of the FIM and the intention of the E-optimality is to maximize the smallest Eigenvalue of the FIM. The advantage of D-optimality is the higher sensitivity to single parameter covariances compared to the A-optimality [36].

With the three common criteria (12)–(14), the process to obtain the optimal excitation signal \mathbf{U} can be depicted in a flowchart, which is shown in Fig. 5.

3.2. Formulation of the optimization problem

The main goal of the optimization is to obtain an excitation sequence, which sufficiently excite the battery cell by high dynamic currents, while the battery constraints are approached simultaneously. In general, constraints on current, battery cell voltage and SoC need to be regarded:

- The current needs to be within minimum/maximum values in order to avoid physical damage or accelerated life time reduction of the battery cell.
- Battery voltage limits of battery cell chemistries, such as lithium polymer and lithium iron phosphate, must be met in order to avoid an explosion due to electrolyte oxidation or fire.
- The SoC of the battery cell is restricted due to the physically defined capacity of the battery cell.

In this paper, two possibilities should be proposed to be used as current constraints in the optimization:

1. High dynamic excitation between physical minimum and maximum current.
2. High dynamic excitation between load (current) ranges, frequently used in operation.

In the first approach, the lower and upper constraints of the current are simply defined at the physical minimum and maximum current. In the second approach, which is used in this paper, the current constraints are defined by analysis of real load cycles: A histogram with a defined number of intervals is used to determine the distribution density of the load. The interval limits of the histogram are used to define the lower and the upper current constraints, while the corresponding distribution densities define the durations within the corresponding constraint ranges. In Fig. 6, a load signal depicted in Subplot (a) with the corresponding histogram depicted in Subplot (b), can be seen. In Subplot (d) the current constraints are depicted. Note that, the advantage of the second approach compared to the first approach is, that the information content is especially increased at operating ranges used in real applications.

The voltage constraints are included indirectly in the current constraints by limiting the minimal/maximal currents depending on the SoC, since the reliability of the output constraints to accurately regard the cell voltage limits using a linear reference model is low. The limitation ratio is depicted in Fig. 6 in Subplot (c). Note that due to the constraints on the current depending on the SoC and the duration within the current limits, the maximal deviation of the SoC from the starting SoC value is limited. Therefore, an adequately chosen starting SoC value defines the SoC limits.

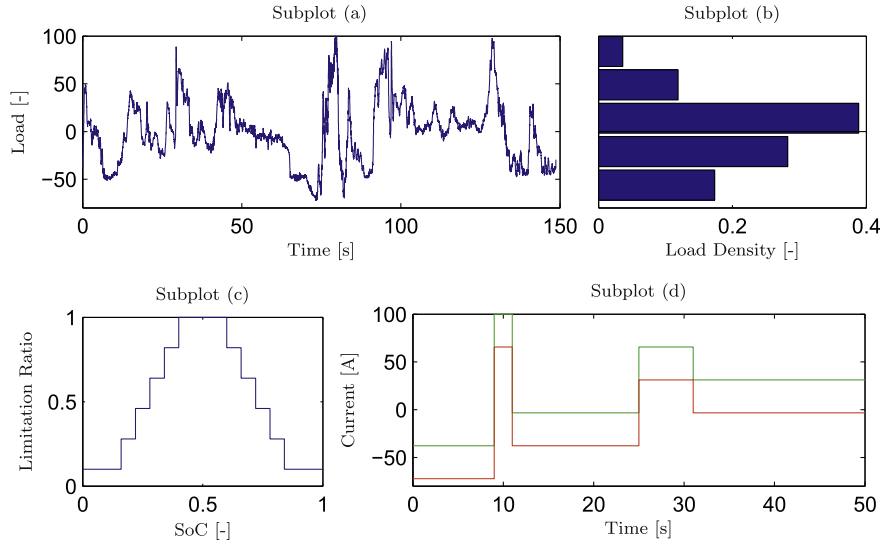


Fig. 6. Construction of the constraints for the optimization. *Subplot (a):* Scaled real load cycle. *Subplot (b):* Histogram of the load density distribution of the real load cycle. *Subplot (c):* Limitation ratio of the applied minimal/maximal physical current depending on the SoC. *Subplot (d):* Current constraints according to the histogram in *Subplot (b)*. Green: upper current constraints. Red: lower current constraints. (For interpretation of the references to colour in this figure legend, the reader is referred to the web version of this article.)

Based on these definitions of the battery constraints, the optimization problem can be formulated: The D-optimality criterion is very much used within optimization problems, due to the invariance by re-parametrization of the model as well as the higher sensitivity to single parameter covariances compared to the A-optimality [32]. Furthermore, in Ref. [4], significant increase in battery model quality has been shown by using the D-optimality criterion. The optimization problem is therefore stated for the D-optimality:

$$\text{D-optimality: } \max_{\mathbf{U}} \det(\mathcal{I}) \quad (15)$$

$$\text{s.t. } \begin{cases} U_{\min}(k) \leq U(k) \leq U_{\max}(k), & k = 1, \dots, N, \\ \mathbf{U} \in \mathbb{R}^{N \times 1} \end{cases}$$

where $U = u_{\text{Current}}$ corresponds to the current input, which is the only degree of freedom of the optimization problem, since the relaxation input and the SoC are directly dependent on the current.

3.3. Constrained optimization

In this paper, the gradient descent method, which has low computational efforts and sufficient performance, is used to solve the stated optimization problem. The gradient $\mathbf{g} = [g(1) \dots g(N)]^T$ is composed of the derivative of the design criterion with respect to the input $U(r)$ for all observations N . The single gradients are obtained by the trace of the product of the derivative of the determinant of the FIM with respect to the parameter sensitivity matrix Ψ and the derivative of Ψ with respect to $U(r)$. The single derivatives are computationally intensive [36] and can be denoted for the r -th observation by

$$\frac{dJ_D(\Psi)}{dU(r)} = \text{Tr} \left(\frac{dJ_D(\Psi)}{d\Psi^T} \frac{d\Psi}{dU(r)} \right), \quad (16)$$

where the first term for the D-optimality is given by (cf. [53])

$$\frac{dJ_D(\Psi)}{d\Psi^T} = 2J_D(\Psi) \Psi [\Psi^T \Psi]^{-1}. \quad (17)$$

Due to the appearance of the inverse of the FIM in Eq. (17), it is important to be mentioned, that the FIM is required to be a regular matrix with full rank.

The second term in Eq. (16) requires to calculate the single derivatives of the parameter sensitivity vectors with respect to the model input, which furthermore is based on the calculation of the derivative of the regressor $\varphi(k, \theta)$ as defined in Eq. (1) with respect to the input $U(r)$, which is denoted by

$$\frac{d\varphi^T(k, \theta)}{dU(r)} = \begin{bmatrix} \frac{d\hat{y}(k-1, \theta)}{dU(r)} \dots \frac{d\hat{y}(k-n, \theta)}{dU(r)} \\ \delta_{1l} \delta_{(k-1)r} \dots \delta_{pl} \delta_{(k-m_l)r} \mathbf{0} \end{bmatrix}, \quad k > r, \quad (18)$$

where δ_{ij} is the Kronecker delta function, l corresponds to the current input of the LMN battery model and the recursive calculation of the former model output with respect to the input $U(r)$ is given by

$$\begin{aligned} \frac{d\hat{y}(k, \theta)}{dU(r)} &= \frac{\partial \hat{y}(k, \theta)}{\partial \hat{y}(k-1, \theta)} \cdot \underbrace{\frac{d\hat{y}(k-1, \theta)}{dU(r)}}_{\text{recursive calculation}} + \dots \\ &+ \frac{\partial \hat{y}(k, \theta)}{\partial \hat{y}(k-n, \theta)} \frac{d\hat{y}(k-n, \theta)}{dU(r)} + \frac{\partial \hat{y}(k, \theta)}{\partial U(r)}, \quad k > r. \end{aligned} \quad (19)$$

The derivative of the parameter sensitivity vector with respect to the model input can then be stated for $k > r$ by

$$\frac{d\psi(k)}{dU(r)} = \begin{bmatrix} \Phi_1(k) \frac{d\varphi(k, \theta)}{dU(r)} \\ \vdots \\ \Phi_M(k) \frac{d\varphi(k, \theta)}{dU(r)} \end{bmatrix} + \begin{bmatrix} \varphi(k, \theta) \frac{d\Phi_1(k)}{dU(r)} \\ \vdots \\ \varphi(k, \theta) \frac{d\Phi_M(k)}{dU(r)} \end{bmatrix}. \quad (20)$$

Summarizing Eq. (20) in a compact notation

$$\frac{d\Psi}{dU(r)} = \left[\frac{d\psi^T(1)}{dU(r)} \dots \frac{d\psi^T(N)}{dU(r)} \right]^T, \quad (21)$$

the second term of Eq. (16) is obtained. Using the calculated gradient \mathbf{g} in the gradient descent method with an adaptively adjusted step size η , the update of the excitation sequence can be formulated to

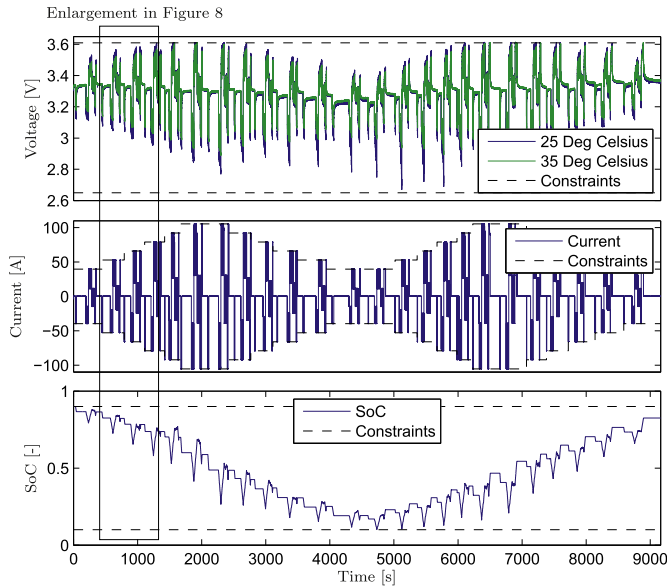


Fig. 7. Optimal excitation signal obtained from optimal model based DoE for Cell **B** depicted for two temperatures.

$$\mathbf{U}^{(v+1)} = \mathbf{U}^{(v)} + \eta \cdot \mathbf{g}^{(v)}, \quad v = 0, 1, 2, \dots \quad (22)$$

$$\text{s.t. } \begin{cases} \mathbf{U}_{\min} \leq \mathbf{U}^{(v+1)} \leq \mathbf{U}_{\max} \\ \mathbf{U} \in \mathbb{R}^{N \times 1} \end{cases}$$

The excitation sequence is updated with the calculated gradient, while the current constraints are applied. This process is repeated until no further improvement is obtained.

Alternatively, the output constraints can be directly included in the optimization problem formulation. Several approaches are available for solving the resulting non-linear constraint

optimization problem: Stadlbauer et al. [36] minimized the (quadratic) difference between the gradient of the design criterion and the excitation signal increment in every iteration, while the feasible area is approached simultaneously. Hametner et al. [38] realized the constrained optimization by Lagrangian multipliers. Other approaches to be applied are sequential quadratic programming (see Ref. [54]) or numerical multi-objective optimization (see Ref. [55]).

3.4. Extensions on the excitation sequence

As introduced at the beginning of this section, the optimized excitation sequence is extended: In front of/after the sequence, constant discharge/charge current with following standby current is added. The value of the constant current is the maximum current dependent on the SoC (see Subplot (c) in Fig. 6). The duration of the constant current is related to the longest time constant of the system. The duration of the standby current need to be a multiple of the duration of the constant current to include sufficient information about relaxation: Compared to Subplot (b) in Fig. 4, at least a duration ratio of 6 is required for an abated voltage degradation at standby current. Therefore, a ratio of 8 is used in this paper.

The final excitation signal is merged by extended high dynamic sequences. The sequences are created for evenly distributed SoC values across the entire SoC range of interest. Depending on the non-road application, the SoC range of interest may vary. It is important to mention, that SoC deviations from the desired SoC, need to be compensated by variation of the durations of the constant currents.

In Fig. 7 the obtained optimal excitation signal is depicted for Cell **B**. Subplot two shows the optimal excitation signal with applied current constraints. The corresponding voltage response is depicted in the first subplot for two different temperatures. As can be seen in the figure, the voltage and SoC constraints are met. Note that the voltage as well as SoC constraints are indirectly regarded due to the current constraints. Also the entire range of SoC required for non-road application is covered.

In Fig. 8 an enlarged view of one extended excitation sequence is depicted. In the second subplot, the current constraints used for the optimization as well as the maximal current depending on the SoC are included. The dynamic current within the lower and upper current constraints (green and red lines) has been optimized by optimal model based DoE. In case of a non-linear reference model used in the optimization, the spread of the current over the dynamic range may also include more intermediate steps [4].

4. Results

In this section, the results of the generically applicable methodology, proposed in this paper, are discussed. It is shown, that the framework of optimal model based design of experiments and the LMN approach can be applied to different battery cells with different cell chemistries. The improvements reached with the optimal excitation signals are presented (Section 4.2), different LMN structures for different cell chemistries are compared to show the influence of the non-linearities (Section 4.3) and the accuracy of the battery model I_5 is discussed in detail on different figures (Section 4.4).

For reproducibility and comparability of the measurements, a defined measurement procedure is applied to the three examined battery cells, which are introduced in the following: Cell **A** is a 40 Ah, prismatic type, energy cell using the lithium polymer chemistry with a nominal voltage of 3.7 V. Cell **B** and **C** are cylindrical type, power cells using the lithium–iron–phosphate cell

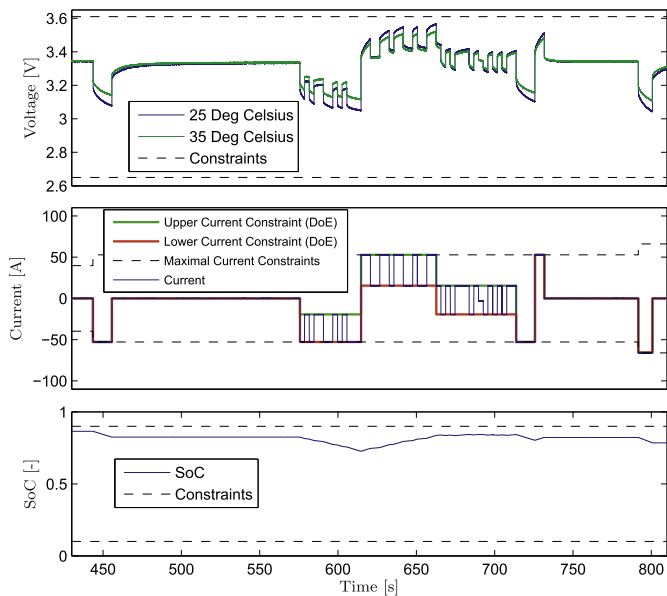


Fig. 8. Enlarged view of the optimal excitation signal in Fig. 7 for Cell **B** at two temperatures. In the second subplot, the current constraints for the optimization (green and red lines) as well as the maximal current constraint depending on the SoC (black dashed lines) are included. (For interpretation of the references to colour in this figure legend, the reader is referred to the web version of this article.)

chemistry with a nominal voltage of 3.3 V. Cell **B** has a capacity of 4.4 Ah and Cell **C** 1.1 Ah, respectively.

The current excitation signals are applied to the battery cells using a battery tester, which is specified in a voltage range of -1 V to 10 V and a current of ± 240 A, while the voltage response as well as the cell temperature are recorded. A Hoecherl&Hackl source/drain module is used for closed-loop current control and a National Instruments USB data acquisition board is used for the measurements. The ambient temperature between 12.5 °C and 35 °C (relevant temperature range for non-road application), which lies within the temperature limits of the battery cells, is controlled by a Vötsch climate chamber. The measurements are executed using a LabView control software, which also monitored battery states and safety issues. The complete system is designed for up to 10 kHz measurements with step response time constants of the source/drain module for less than 200 μ s in order to fulfill the high dynamic requirements of non-road applications. All measurements have been recorded with a sampling rate of 100 Hz, which simultaneously is the sampling rate of all models.

4.1. Measurement procedure

In order to guarantee reproducibility as well as to exclude different initial battery conditions as the reason for unexpected and undefined appearing effects in measurements, it is made use of a defined measurement procedure. All different cell chemistries are examined based on this procedure, which erases all short term history of the battery cells (cell conditioning). Furthermore, the procedure is required for comparison between different battery cells and chemistries, respectively. It is established as follows:

1. Initial capacity check at 25 °C
2. Set temperature of climate chamber
3. Fully charge the battery cell
4. Discharge until initial SoC is reached
5. Apply excitation signal
6. Repeat 3 to 5 until all excitation signals are recorded
7. Repeat 2 to 6 until all temperatures are recorded

The initial capacity check (see enumeration (1)), is applied only once to obtain the true capacity and in order to reduce the influence of the short term history on the battery cell. The capacity is calculated by the last of 8 applied charge/discharge cycles with different C-rates from $4C$ to $1C$. Additionally, the charge efficiencies can be obtained by the difference between the quotient of discharge capacity divided by charge capacity.

4.2. Battery model quality improvement with optimal model based design of experiments

The benefit due to optimal excitation signals should be shown by comparison of two local model networks (models Γ_1 and Γ_2) with the same configuration, but identified using training data from conventional DoE and optimal model based DoE, respectively. In order to exclusively show the effect of the training data, the models are only parameterized for a simplified LMN structure.

The partition space of the models is defined by $\mathcal{Z}_{12} = [z_{\text{SoC}} \ z_{\text{Hyst}}]$ since the temperature is hold constant at 22.5 °C and the input space is defined by $\mathcal{Q}_{12} = [u_{\text{Current}}]$ because SoC and the relaxation parameter are neglected in the models. The model orders of current and voltage are found by comparing the mean squared error of a linear model for different selections of the order [45]. A good compromise between complexity and accuracy is chosen to $m_{\text{Current}} = n_{\text{Voltage}} = 5$.

Table 1

Summary of the LMN configuration parameters of models Γ_1 and Γ_2 , which are used to compare the benefits of optimal model based DoE to conventional DoE. The model parameters are identified by different training data at 22.5 °C temperature (c.f. Figs. 9 and 10).

LMN structure	Configuration parameters
$\mathcal{Z}_{12} = [z_{\text{SoC}} \ z_{\text{Hyst}}]$	$m_{\text{Current}} = n_{\text{Voltage}} = 5$
$\mathcal{Q}_{12} = [u_{\text{Current}}]$	$k_{\sigma, \text{SoC}, 12} = 0.75$
	$k_{\sigma, \text{Hyst}} = 0.05$
	$M = 30$

For the given partition space, the kernel function sharpness of the SoC is found by comparing the suitability of a LMN model with 10 local linear models at different selections of the sharpness factor $k_{\sigma, \text{SoC}}$. A good compromise between smoothness and strict partitioning is chosen at $k_{\sigma, \text{SoC}, 12} = 0.75$. Note here that a smaller value of k_{σ} reduces the overlapping of the validity functions. The sharpness factor for the hysteresis input is set to $k_{\sigma, \text{Hyst}} = 0.05$ since a sharp separation is preferable, because smoothness between discharge and charge behavior is not physically reasonable. The number of LLM is defined to the threshold $M = 30$ since this is the real time capability limit obtained by test runs on a battery emulator control unit² (Beckhoff Industrial PC C6515). The LMN configuration parameters for models Γ_1 and Γ_2 are summarized in Table 1.

Fig. 9 depicts the raw data of the training data obtained by conventional DoE for Cell **C** which is used to identify the parameters for model Γ_1 . The step profile training data is similar to the asymmetrical step profile mentioned in Ref. [29] and is more dynamic compared to the other observed excitation signals in the literature [4]. Therefore it is taken for comparison with the optimal model based DoE excitation signal, which belongs to the group of high dynamic excitation signals. The step profile is constructed by merging alternating intermediate current steps in charge and discharge direction. Due to the variation of the step durations, the entire SoC range is covered. Because of the strict DoE, the voltage behavior is not directly considered. This leads to voltage violations, if the current is not limited by expert knowledge. The applied current constraints are depicted in the second subplot. Due to the limitation of the current, the voltage and SoC constraints are met. The full current capability of the battery cell cannot be achieved with this excitation signal.

The parameters of model Γ_2 are identified by an optimal excitation signal which is obtained from optimal model based DoE for Cell **C**. In Fig. 10, the raw data of the optimal excitation signal is depicted. In general only current constraints are applied to the optimal model based DoE, while voltage as well as SoC constraints are indirectly regarded in the current constraints. The training result of model Γ_2 is included in the first subplot. Compared to the step profile in Fig. 9, the dynamics of the optimal excitation signal is higher and the current in the middle of the SoC range is bigger, though all constraints are met. Note that the signal is obtained by adapting the methodology described in Section 3 for the capabilities of Cell **C**.

The accuracies of the models are validated by a repeated real (current-) load cycle, which represents the high dynamic requirements of non-road applications. During the load cycle, on average, the battery cell is not charged/discharged, which makes repetitions of the cycle possible. The entire SoC range is covered by alternatingly raising/lowering the mean current value of the cycle, which charges/discharges the battery cell on average. This validation signal is referred to as *SoC validation signal*. Note that, the

² CPU usage of the battery model with 30 LLM is between 8 and 12%, which is the critical limit for real time usage in a battery emulator.

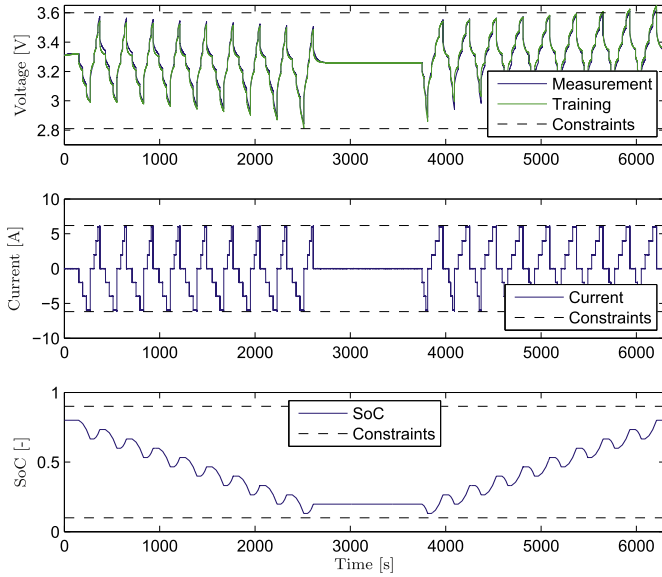


Fig. 9. Step profile training data adapted for Cell C to be used for the parameter identification of model Γ_1 . The temperature is held at 22.5 °C. The training result of model Γ_1 is included in the first subplot.

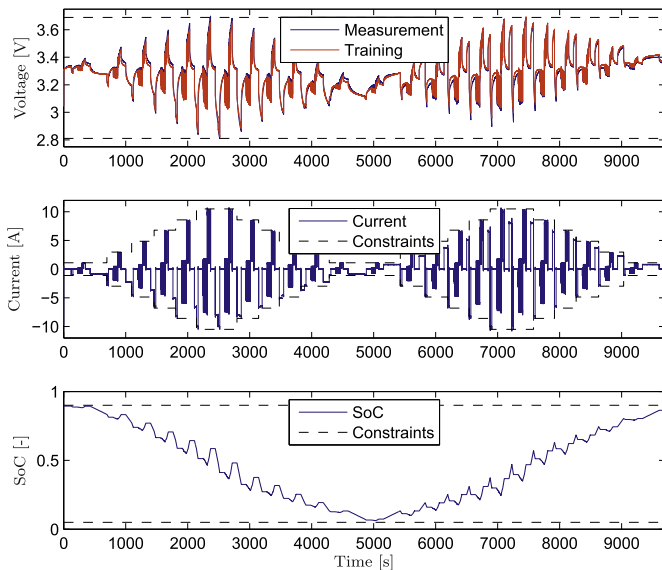


Fig. 10. Optimal excitation signal training data for Cell C at 22.5 °C to be used for the parameter identification of model Γ_2 . The training result of the model is included in subplot one.

ambient temperature is also kept constant during the experiment (22.5 °C) and in order to match the full current capability of the battery cell, the real load cycle is scaled to the maximum current allowed for Cell C. The simulation result of the SoC validation signal, is depicted in Fig. 11. The SoC trajectory can be seen in the last subplot.

Comparing the envelope curves of the maximal voltage values in Fig. 11, it can be noticed, that both models include the non-linear relationship of SoC and battery cell voltage, though the average error of model Γ_1 (56.25 mV) is significantly bigger than the error of model Γ_2 (5.44 mV). In Fig. 12, an enlarged view of one real load cycle in Fig. 11, is depicted.

The dynamic behavior of the models Γ_1 and Γ_2 are similar, as can be seen in the first subplot of Fig. 12, but model Γ_1 has a large offset

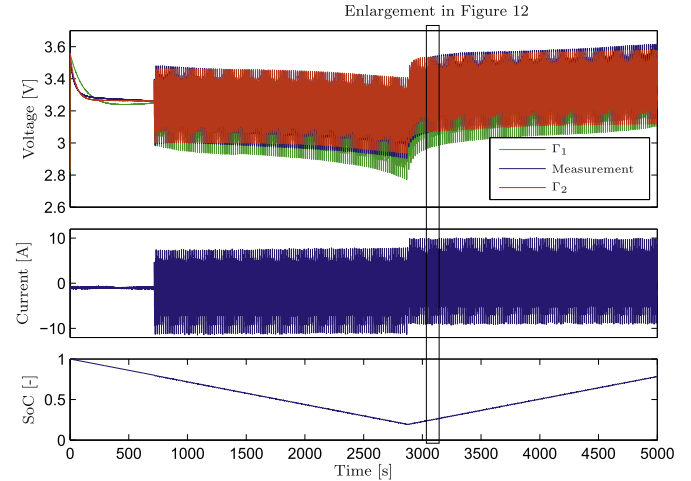


Fig. 11. Simulation result comparison of models Γ_1 and Γ_2 , shown on a SoC validation signal measured on Cell C at 22.5 °C. The signal is based on a real load cycle, which represents the high dynamic requirements of non-road applications. The envelope curves of the maximal voltage values show a significant higher error of model Γ_1 .

compared to model Γ_2 . This is caused by the lack of high dynamic excitation included in the step profile training data of model Γ_1 . The optimal excitation signal leads to a significant increase in the model accuracy at high dynamic excitation of the battery cells. Note that, though, the maximum C-rate of the signal is above 9C, the accuracy of model Γ_2 is still satisfactory.

In the following, a more detailed discussion of the LMN approach for battery modeling is based on battery models trained with optimal excitation signals, exclusively.

4.3. Comparison of battery models with different LMN structures and cell chemistries

In this section, three different LMN battery models (Γ_3 , Γ_4 , Γ_5) are compared with each other based on two different validation signals. The models differ in the LMN structure to show the influence of hysteresis and relaxation input on the model accuracy, while the temperature is regarded simultaneously. Furthermore, the models are identified for two different battery cells (Cell A with lithium polymer and Cell B with lithium–iron–phosphate chemistry) to emphasize the cell chemistry independence of the LMN approach.

The model parameters of the models (Γ_3 , Γ_4 , Γ_5) are identified by the same training data obtained by optimal model based DoE (see Fig. 7 for an optimal excitation signal of Cell B at two temperatures). The optimal excitation signal is measured at 10 different temperatures between 12.5 °C and 35 °C in 2.5 °C steps and is then merged to one training data set (raw data for identification). The same is done for Cell A and B, respectively.

The LMN structures and configuration parameters of the models are summarized in Table 2. The simplest model (Γ_3) does not regard the hysteresis and relaxation effects, in order to see an improvement due to the hysteresis and relaxation input. The partition and input space are defined by $\mathcal{Z}_3 = [\mathcal{Z}_{\text{SoC}} \mathcal{Z}_{\text{Current}} \mathcal{Z}_{\text{Temp}}]$ and $\mathcal{Q}_3 = [\mathcal{Z}_{\text{SoC}} u_{\text{Current}}]$, respectively. Note that the current $\mathcal{Z}_{\text{Current}}$ is only interpolated between the charge/discharge behavior at standby current and does not refer to the corresponding polarization of the battery cell. The initial partition of the current input is therefore split between positive/negative current instead of charge/discharge mode. Nevertheless, in model Γ_3 the current effects are included by $\mathcal{Z}_{\text{Current}}$. The SoC \mathcal{Z}_{SoC} in the input space is included due

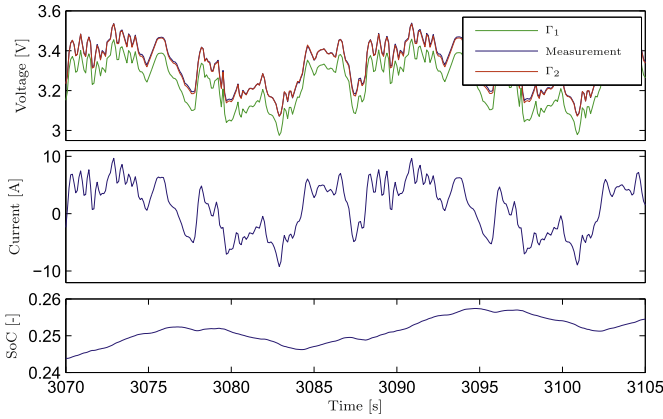


Fig. 12. Enlarged view of Fig. 11: The comparison of models I_1 and I_2 at one real load cycle measured on Cell C at 22.5 °C. Significantly accuracy increase due to high dynamic training data observable for model I_2 .

Table 2

Summary of the LMN configuration parameters of models I_3 , I_4 and I_5 . The influence of the hysteresis as well as relaxation input on the model accuracy is illustrated by different Z and Q . The model parameters are identified by the same training data (c.f. Fig. 7).

LMN structure for I_3 , I_4 and I_5		
I_3	$Z_3 = [Z_{SoC} \ Z_{Current} \ Z_{Temp}]$	$Q_3 = [Z_{SoC} \ u_{Current}]$
I_4	$Z_4 = [Z_{SoC} \ Z_{Hyst} \ Z_{Temp}]$	$Q_4 = [Z_{SoC} \ u_{Current}]$
I_5	$Z_5 = [Z_{SoC} \ Z_{Hyst} \ Z_{Temp}]$	$Q_5 = [Z_{SoC} \ u_{Current} \ u_{Relax}]$
Configuration parameters for I_3 , I_4 and I_5		
$m_{SoC} = 1$	$k_{\sigma, SoC, 345} = k_{\sigma, Temp} = 0.6$	
$m_{Relax} = 3$	$k_{\sigma, Hyst} = k_{\sigma, Current} = 0.05$	
$m_{Current} = n_{Voltage} = 5$	$M = 30$	

to the continuous change of the voltage depending on the SoC as well as the requirement for state observer design (c.f. [11]).

In Model I_4 , the current input is replaced by the hysteresis input in order to regard the hysteresis effect. The partition space is defined by $Z_4 = [Z_{SoC} \ Z_{Hyst} \ Z_{Temp}]$, while the input space is $Q_4 = Q_3$.

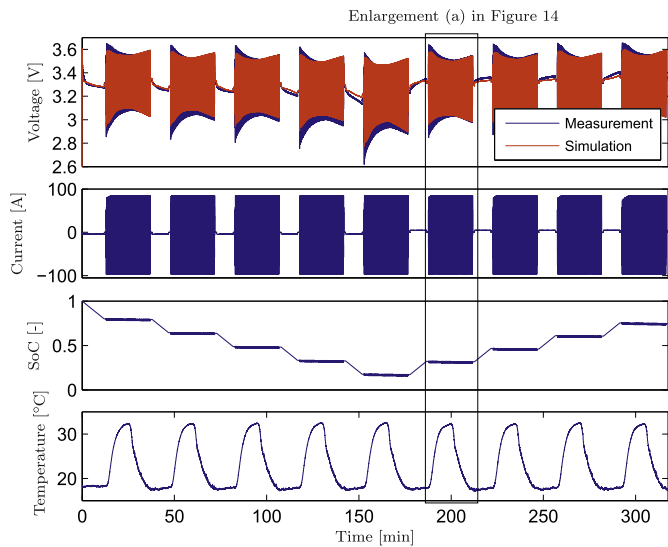


Fig. 13. Resulting plot of the temperature validation signal applied to Cell B and the simulated cell voltage using model I_5 . The real load cycle is repeated at different SoC levels while the ambient temperature is heated up to the upper level of 32 °C and cooled back to the lower level of 18 °C.

Note that the complexity of the model does not change in this case. Additionally to the configuration of model I_4 , the relaxation input is included in the input space of model I_5 . The input space follows to $Q_5 = [Z_{SoC} \ u_{Current} \ u_{Relax}]$, while the partition space is $Z_4 = Z_5$. Note here, that the model complexity is increased by the relaxation parameter. Model I_5 includes all relevant electrochemical effects discussed in the manuscript.

The configuration parameter objectives for models I_3 , I_4 and I_5 does not change in principle to those of models I_1 and I_2 and therefore $m_{Current} = n_{Voltage} = 5$, $k_{\sigma, Hyst} = 0.05$ and $M = 30$ can be directly taken from Table 1. The sharpness factor for the current input is set to $k_{\sigma, Current} = k_{\sigma, Hyst} = 0.05$, since a sharp separation between charge and discharge behavior is preferable. The optimal kernel function sharpness of the SoC and temperature is found to be $k_{\sigma, SoC, 345} = k_{\sigma, Temp} = 0.6$, because the temperature input slightly increase the smoothness of the validity function. The remaining model order of the SoC input is set to $m_{SoC} = 1$, due to no dynamic influence on the system behavior and the order of the relaxation input is set to $m_{Relax} = 3$, because $filt(\cdot)$ is designed by a third order low pass filter.

The validation of the battery models is done with a *temperature validation signal* and the *SoC validation signal*: In the temperature validation signal, the aforementioned real load cycle is repeated at a defined SoC level until the ambient temperature is heated up to the upper level of 32 °C and cooled back to the lower level of 18 °C. The same procedure is applied for different SoC levels. The influence of the SoC is validated with a slightly changed SoC validation signal as introduced in Section 4.2: In order to strengthen the significance of the validation, the current mean value of the cycle is more often raised/lowered in between the signal. Note that, the average charge direction is therefore changed more often compared to the SoC validation signal used in Section 4.2. Nevertheless, the entire SoC range is covered. The *temperature validation signal* and the *SoC validation signal* are depicted in Figs. 13 and 15, respectively. A more detailed description is given in the next section.

The model accuracy is evaluated using the mean squared error (MSE) and a normalized root mean squared error (NRMSE) as given in Eq. (23)

$$e_{NRMSE, \%} = \sqrt{\frac{1}{N_s} \sum_{i=1}^{N_s} \left(\frac{y_i - \hat{y}_i}{\max(y) - \min(y)} \right)^2} \cdot 100\%, \quad (23)$$

where N_s is the number of samples, y is the measured output and \hat{y} is the simulated output. Note that, the normalization in Eq. (23) is done by the measured output values of the specified validation signal, which permits the comparison of the different battery model accuracies. In Table 3 the simulation error values of the different LMN architectures and cell chemistries are depicted.

In Table 3, it is observable in the MSE as well as NRMSE values, that hysteresis and relaxation input, respectively, increase the battery model accuracy of both cell chemistries. The current input in model I_3 only interpolates between the charge/discharge behavior at standby current, which is not physically appropriate. In contrast, the hysteresis input refers to the corresponding polarization if the current is going to zero, which reflects the electrochemical behavior of battery cells more than the current input. Therefore the accuracy of model I_4 is increased.

Electrochemical batteries usually have very different time constants in the dynamic behavior. Measurements need to be recorded with a high sampling rate, as otherwise the fast dynamic behavior is not included in the recorded data. Due to the fast sampling rates, the data get highly correlated and therefore numerical problems due to ill-conditioning arise at the parameter estimation [56,57]. This phenomenon is referred to as *redundance* [56]. Since the

Table 3

Validation error values for the LMN battery models Γ_3 , Γ_4 and Γ_5 as defined in Table 2. The error values are shown for Cell A and B, respectively. Comparing the models with each other, independent from the cell chemistry, model Γ_5 has the best model accuracy, model Γ_3 the worst and model Γ_4 denotes intermediate accuracy.

Battery cell		Cell A		Cell B	
Criterion		MSE	NRMSE	MSE	NRMSE
Temp. Val. Sig.	Γ_3	$2.935e^{-4}$	2.059%	$7.592e^{-4}$	2.671%
	Γ_4	$2.668e^{-4}$	1.963%	$6.585e^{-4}$	2.487%
	Γ_5	$2.447e^{-4}$	1.752%	$5.236e^{-4}$	2.218%
SoC Val. Sig. 20 °C	Γ_3	$3.711e^{-4}$	2.537%	$5.652e^{-4}$	2.933%
	Γ_4	$3.559e^{-4}$	2.485%	$4.811e^{-4}$	2.706%
	Γ_5	$1.431e^{-4}$	1.438%	$3.386e^{-4}$	2.270%
SoC Val. Sig. 25 °C	Γ_3	—	—	$4.622e^{-4}$	2.928%
	Γ_4	—	—	$4.094e^{-4}$	2.756%
	Γ_5	—	—	$3.109e^{-4}$	2.402%
SoC Val. Sig. 30 °C	Γ_3	—	—	$3.633e^{-4}$	2.847%
	Γ_4	—	—	$3.393e^{-4}$	2.752%
	Γ_5	—	—	$2.496e^{-4}$	2.360%

model is sampled with 100 Hz, it is very difficult to identify the corresponding relaxation time constant precisely within the dynamic behavior. Therefore, further improvement is achieved by inserting the relaxation input to the input space of model Γ_5 .

Comparing the MSE/NRMSE values of the three discussed models (Γ_3 , Γ_4 , Γ_5) in Table 3, the best accuracy is obtained by model Γ_5 while the worst is obtained by model Γ_3 .

4.4. Detailed discussion of LMN battery model Γ_5

In the following, since model Γ_5 includes all relevant electrochemical effects and showed the best accuracy in the comparison, the relaxation, hysteresis and temperature influence should be discussed in more detail based on model Γ_5 . The system behaviors of the different cell chemistries in this paper are similar and therefore the resulting plots are only shown for the measurements of Cell B. In Fig. 13, the temperature validation signal is depicted. In subplot three and four, the SoC as well as temperature trajectory can be seen, respectively.

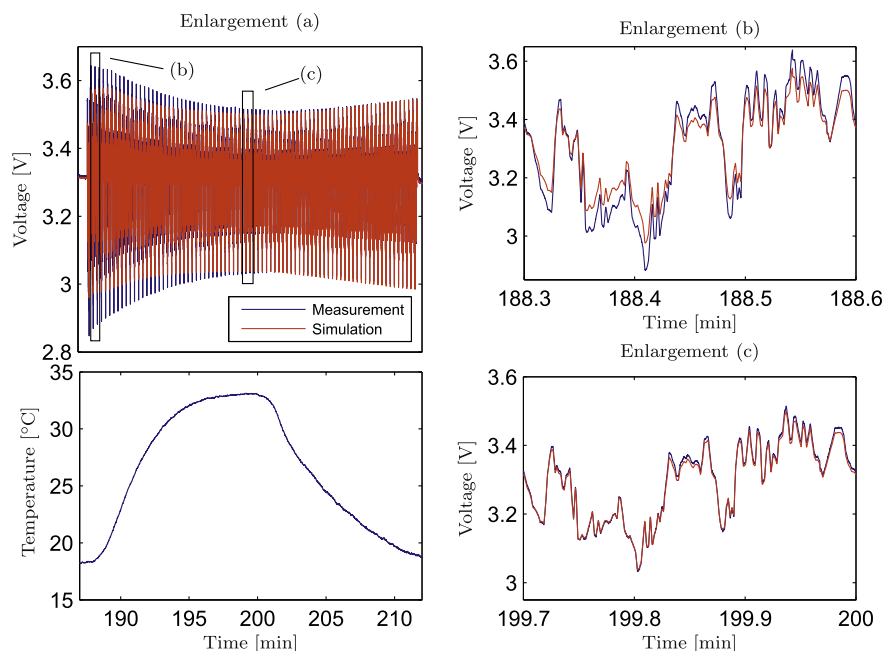


Fig. 14. Resulting enlargement plots of the temperature validation signal (see Fig. 13) applied to Cell B. Enlargements (b) and (c) as defined in (a).

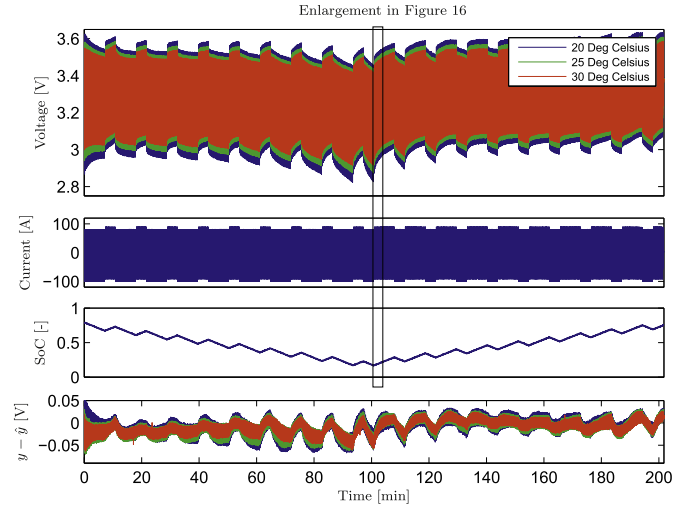


Fig. 15. Resulting plot of the SoC validation signal applied to Cell B at three different ambient temperatures (20 °C, 25 °C and 30 °C). An enlarged view of the marked region is depicted in Fig. 16.

The first subplot in Fig. 13 shows the voltage response of the cell terminal voltage and the simulated cell voltage using model Γ_5 . It can be observed, that the model output changes depending on the ambient temperature. The model mismatch at the beginning of the dynamic excitation at the different SoC levels comes from a changing time constant of the relaxation effect. Since the time constant of the filter input is kept constant, this effect is not regarded in the model. Nevertheless, the model accuracy is significantly increased by the relaxation input (c.f. Table 3). For the SoC transition between the repeated load cycles, low constant current is used, while in non-road applications usually high battery currents (more than 20C) occur. The lack of sufficient information at low constant current (below 2C) within the training data explains the small model mismatch at the transition. The hysteresis effect is due to the continuous change between charge and discharge not

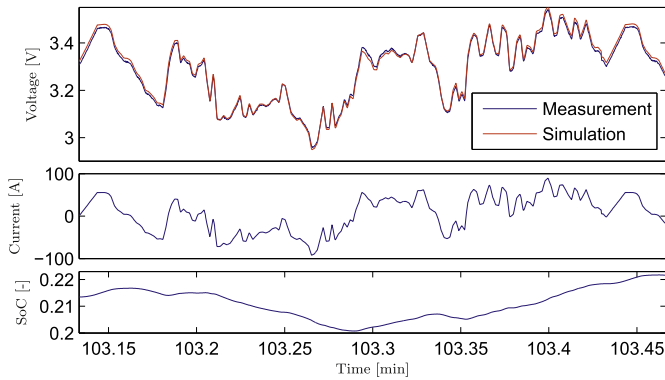


Fig. 16. Enlarged view of marked region in Fig. 15. One real load cycle applied to Cell B at 30 °C ambient temperature. Simulation result of battery model I_5 at applied current rates above 20C.

directly observable in Fig. 13. Comparing the error values in Table 3, the improvement due to the hysteresis input, can be verified explicitly. In Fig. 14, the enlargement of the marked region is depicted.

In enlargements (b) and (c) in Fig. 14, one enlarged load cycle is depicted for the marked regions in enlargement (a). It can be seen, that the dynamics required for non-road applications are met by the model. Comparing enlargements (b) and (c), the effect of the mentioned changing time constant of the relaxation effect can be observed by the slightly bigger voltage error in enlargement (b).

The validation of the SoC influence is depicted in Fig. 15. The SoC validation signal is repeated for 20 °C, 25 °C and 30 °C constant ambient temperature to show the SoC influence at different temperatures.

The invariant error on the changing SoC in Fig. 15 Subplot 4, show the non-linear consideration of the SoC by the battery model. The voltage errors at the different temperatures, depicted in Subplot 4, are all within a small tolerance tube of less than a maximum error of 90 mV, which shows the good accuracy of the model at different temperatures. Note that, the current rates are above 20C, which can be seen in Fig. 16, where an enlarged view of one load cycle is depicted at low SoC.

In Fig. 16, one real load cycle is depicted for a low SoC value at 30 °C ambient temperature. Though, the voltage behavior at low SoC and high current values (above 20C) is strongly non-linear, the model is able to represent the underlying behavior of the battery cell, accurately.

5. Conclusion

In this paper, a generic methodology for non-linear system identification of electrochemical battery cells is presented. The local model network approach is applied to model the battery cell terminal voltage. The relaxation and hysteresis effects as well as the SoC, current and temperature are regarded in the LMN by corresponding inputs. The LMN is constructed with an enhanced LOLI-MOT algorithm, which uses predefined partitions and reduced partitioning dimensions to obtain a physically appropriate network. Optimal model based design of experiments is utilized to create optimal excitation signals, which increase the information content of measurements. The excitation signals are optimized for load ranges frequently used in real load cycles. The results indicated that a simple linear reference model, used in the optimization of the excitation signal, could already increase the model accuracies significantly. The battery model errors for validation signals with currents above 20C have been below 3% NRMSE. The high model accuracies could be achieved for different battery cell chemistries

and temperatures. A defined measurement procedure guaranteed the reproducibility as well as comparability of the results and the real time capability of the battery model is demonstrated on an industrial PC.

References

- [1] C. Hametner, S. Jakubek, J. Power Sources 238 (0) (2013) 413–421, <http://dx.doi.org/10.1016/j.jpowsour.2013.04.040>.
- [2] Y. Hu, S. Yurkovich, J. Power Sources 198 (2012) 338–350.
- [3] G. Plett, J. Power Sources 134 (2) (2004) 277–292.
- [4] J. Unger, C. Hametner, S. Jakubek, M. Quasthoff, in: Electrical Systems for Aircraft, Railway and Ship Propulsion (ESARS), IEEE, 2012, pp. 1–6.
- [5] L. Gao, S. Liu, R. Dougal, IEEE Trans. Compon. Packag. Technol. 25 (3) (2002) 495–505.
- [6] B. Pattipati, C. Sankavaram, K.R. Pattipati, IEEE Trans. Syst., Man, Cybern. C Appl. Rev. (2010) 1–16, <http://dx.doi.org/10.1109/TSMCC.2010.2089979>.
- [7] J. Gomez, R. Nelson, E.E. Kalu, M.H. Weatherspoon, J.P. Zheng, J. Power Sources 196 (10) (2011) 4826–4831.
- [8] R. Klein, N. Chaturvedi, J. Christensen, J. Ahmed, R. Findeisen, A. Kojic, in: American Control Conference, IEEE, 2010, pp. 6618–6623.
- [9] M. Doyle, T. Fuller, J. Newman, J. Electrochem. Soc. 140 (6) (1993) 1526–1533.
- [10] S. Santhanagopalan, R. White, J. Power Sources 161 (2) (2006) 1346–1355.
- [11] N. Chaturvedi, R. Klein, J. Christensen, J. Ahmed, A. Kojic, IEEE Control Syst. Mag. 30 (3) (2010) 49–68.
- [12] G. Plett, J. Power Sources 134 (2) (2004) 252–261.
- [13] G. Plett, J. Power Sources 134 (2) (2004) 262–276.
- [14] M. Charkhgard, M. Farrokhi, IEEE Trans. Indus. Electron. 57 (12) (2010) 4178–4187.
- [15] L. Wang, Adaptive Fuzzy Systems and Control: Design and Stability Analysis, Prentice Hall, 1994.
- [16] J. Wang, Q. Chen, Adv. Neural Networks (2005) 199–221.
- [17] Z. Jing, A. Luo, M. Tomizuka, Int. J. Intell. Control Syst. 3 (2) (1998) 193–203.
- [18] J. Wang, L. Xu, J. Guo, L. Ding, Proc. Inst. Mech. Eng. D J. Automob. Eng. 223 (1) (2009) 27–35.
- [19] L. Xu, J. Wang, Q. Chen, Energy Convers. Manag. 53 (1) (2012) 33–39.
- [20] C. Hametner, S. Jakubek, in: American Control Conference, IEEE, 2007, pp. 864–869.
- [21] R. Murray-Smith, T. Johansen, Multiple Model Approaches to Nonlinear Modelling and Control, CRC Press, 1997.
- [22] G. Gregorčic, G. Lightbody, IEEE Trans. Neural Networks 18 (5) (2007) 1404–1423.
- [23] R. Kroeze, P. Krein, in: Power Electronics Specialists Conference, IEEE, 2008, pp. 1336–1342.
- [24] M. Chen, G. Rincon-Mora, IEEE Trans. Energy Convers. 21 (2) (2006) 504–511.
- [25] A. Hentunen, T. Lehmuspelto, J. Suomela, in: Vehicle Power and Propulsion Conference (VPPC), IEEE, 2011, pp. 1–6.
- [26] K. Smith, C. Rahn, C. Wang, IEEE Trans. Control Syst. Technol. 18 (3) (2010) 654–663.
- [27] Y. Hu, S. Yurkovich, Y. Guezennec, B. Yurkovich, J. Power Sources 196 (1) (2011) 449–457.
- [28] Y. Hu, B. Yurkovich, S. Yurkovich, Y. Guezennec, in: Dynamic Systems and Control Conference, ASME, 2009, pp. 233–240.
- [29] Y. Hu, S. Yurkovich, Y. Guezennec, B. Yurkovich, Control Eng. Pract. 17 (10) (2009) 1190–1201.
- [30] K. Smith, C. Wang, J. Power Sources 160 (1) (2006) 662–673.
- [31] F. Sun, R. Xiong, H. He, W. Li, J. Aussems, Appl. Energy 96 (2012) 378–386.
- [32] L. Pronzato, Automatica 44 (2) (2008) 303–325.
- [33] B. Hartmann, J. Moll, O. Nelles, C. Fritzen, in: IEEE International Conference on Control Applications, IEEE, 2011, pp. 1163–1170.
- [34] D. Cohn, Neural Networks 9 (6) (1996) 1071–1083.
- [35] M. Defforian, F. Klöpper, in: Design of Experiments (DoE) in Engine Development, vol. 4, 2009, pp. 31–40.
- [36] M. Stadlbauer, C. Hametner, S. Jakubek, in: Proceedings of the IASTED International Conference in Control and Applications, vol. 20, 2011.
- [37] M. Stadlbauer, C. Hametner, S. Jakubek, T. Winsel, in: Proceedings of the Eighth IFAC World Congress, 2011, pp. 4332–4337.
- [38] C. Hametner, M. Stadlbauer, M. Derregnaucourt, S. Jakubek, T. Winsel, Eng. Appl. Artif. Intell. 26 (1) (2013) 251–261, <http://dx.doi.org/10.1016/j.engappai.2012.05.016>.
- [39] C. Hametner, J. Unger, S. Jakubek, in: 12th WSEAS International Conference on Robotics, Control and Manufacturing Technology (ROCOM'12), WSEAS, 2012, pp. 116–123.
- [40] O. Nelles, Nonlinear System Identification: from Classical Approaches to Neural Networks and Fuzzy Models, Springer, Berlin, 2001.
- [41] O. Nelles, R. Isermann, in: Proceedings of the 35th IEEE Decision and Control, vol. 1, IEEE, 1996, pp. 470–475.
- [42] R.B. D'Agostino, Goodness-of-Fit-Techniques, vol. 68, CRC Press, 1986.
- [43] J.M. De Sá, Applied Statistics: Using SPSS, Statistica, MATLAB, and R, second ed., Springer, 2007.
- [44] S. Yuan, H. Wu, C. Yin, Energies 6 (1) (2013) 444–470, <http://dx.doi.org/10.3390/en6010444>.

- [45] R. Jackey, M. Saginaw, P. Sanghvi, J. Gazzarri, T. Huria, M. Ceraolo, SAE Tech. Pap. 2013-01-1547, 2013, <http://dx.doi.org/10.4271/2013-01-1547>.
- [46] F. Hoffmann, O. Nelles, *Inf. Sci.* 136 (1) (2001) 7–28.
- [47] S. Jakubek, N. Keuth, *Eng. Appl. Artif. Intell.* 19 (6) (2006) 705–717.
- [48] S. Jakubek, C. Hametner, *IEEE Trans. Syst., Man, Cybern. B Cybern.* 39 (5) (2009) 1121–1133.
- [49] S. Abu-Sharkh, D. Doerffel, J. Power Sources 130 (1–2) (2004) 266–274.
- [50] D. Bernardi, J. Go, J. Power Sources 196 (1) (2011) 412–427.
- [51] X. Tang, X. Zhang, B. Koch, D. Frisch, in: *International Conference on Prognostics and Health Management*, IEEE, 2008, pp. 1–12.
- [52] G. Goodwin, R. Payne, *Dynamic System Identification: Experiment Design and Data Analysis*, Academic Press Inc., New York, 1977.
- [53] J. Magnus, H. Neudecker, *Matrix Differential Calculus with Applications in Statistics and Econometrics*, second ed., Wiley, 1988.
- [54] D. Luenberger, Y. Ye, *Linear and Nonlinear Programming*, third ed., Springer, 2008.
- [55] M. Seyr, S. Jakubek, in: *American Control Conference*, IEEE, 2007, pp. 3336–3341.
- [56] S. Billings, L.A. Aguirre, *Int. J. Bifurcat. Chaos* 5 (06) (1995) 1541–1556.
- [57] L. Ljung, *System Identification*, Springer, 1998.